energy (equation 2.4) with respect to displacement of the plate, it is possible to obtain the induced electrostatic force F_E as follows:

$$F_E = \frac{1}{2}\frac{\xi_0 A V^2}{(g_0 - w)^2}. \tag{2.5}$$

The force of a linear spring with spring constant k is equal to:

$$F_K = kw. \tag{2.6}$$

In equilibrium the electrostatic force F_E and spring force F_K are equal. Consequently the induced displacement w in the plate is proportional to the square of the applied voltage V. For more details regarding electrostatic actuation and different configurations in MEMS refer to *Microsystem Design* [35, ch. 6]. A simplified analytical derivation for the deformations in a electrostatic actuated deformable mirror can be found in [26].

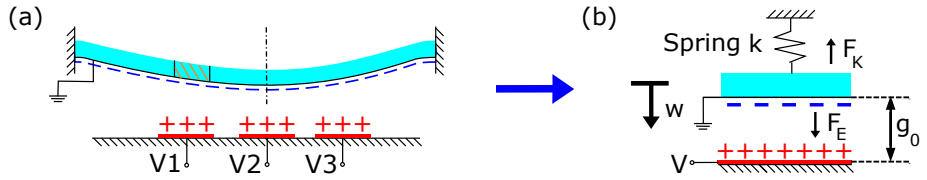

Figure 2.3. Electrostatic actuation concept. (a) Attraction force between oppositely charged surfaces and (b) simplified parallel-plate and spring actuator model for the shaded element in (a).

2.2. Spatial-carrier fringe-pattern analysis for surface measurement

For performing wavefront measurement and consequently characterizing the fabricated opto-fluidic deformable membranes, an interferometry-based measurement system is developed. In this section, briefly the idea of employed interferometer is discussed and then the algorithm of spatial-carrier fringe-pattern analysis for quantitative phase measurement is introduced.

2.2.1. Mach-Zehnder interferometer

Interferometers with different configurations are an important group of precise optical measurement setups both in macro and micro scales [36, p. 136]. Interference happens when two waves (here electromagnetic waves), that are coherent, meet. For more details on the derivation of the superimposed field and intensity refer to [37, ch. 9].

Among different configurations of interferometers, Mach-Zehnder has a special two-beam arrangement making it suitable for measuring Optical Path Difference (OPD) caused by a transparent refractive element that is fixed in one of the interferometer arms (measurement arm). As it can be seen in figure 2.4, first coherent light from a laser is collimated and then split into two beams at beam splitter α; namely reference beam and the measurement beam. The measurement beam interacts with the refractive opto-fluidic membrane. The shape of the membrane changes the amount of liquid in path of the laser beam, which results in an effective change in the optical path length because of the higher refractive index of the liquid n_l with respect to that of air n_{air}. The 2 beams recombine at the second beam splitter β and interfere. The modulation of the intensity induced due to interference with a phase shift of $\Delta\phi$ at each point of the beam may be calculated with the following [36, p. 142]:

$$I = \frac{I_0}{2}\left(1 + \cos\Delta\phi\right) = \frac{I_0}{2}\left[1 + \cos\left(\frac{2\pi h_l \Delta n}{\lambda_0}\right)\right], \tag{2.7}$$

where $\Delta\phi$ is equal to:

$$\Delta\phi = \left(\frac{2\pi h_l \Delta n}{\lambda_0}\right). \tag{2.8}$$

I_0 is the intensity of light source, h_l is the height of liquid at each point of the membrane surface, Δn is the difference between refractive indices and λ_0 is the wavelength of light source in vacuum. It is worth mentioning that if the refractive element was not in the measurement path, the output interferogram would be a series of parallel fringe lines with a period that is a function of the relative angle between the plane mirrors (no fringe for zero relative angle).

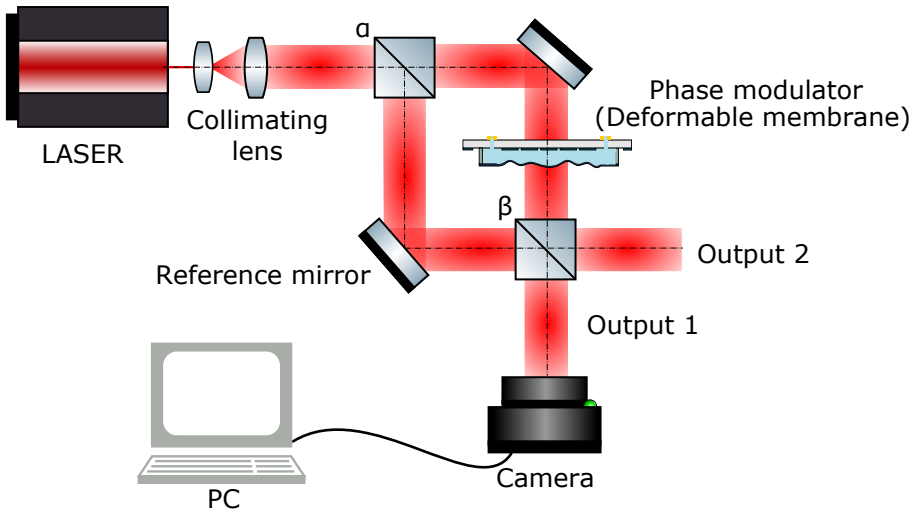

Figure 2.4. Schematic representation of Mach-Zehnder interferometer used in proposed measurement system.

2.2.2. Spatial-carrier fringe-pattern analysis algorithm

There are two major strategies to analyze interferometric data in to quantitative phase data. Temporal Phase Measurement (TPM) methods use a phase shifting that requires at least three intesnity measurements and an actuator for shifting the phase. Such a system is not suitable to implement for a real-time setup. Spatial Phase Measurement (SPM) methods on the other hand can capture the required data in a single frame with a spatial-carrier and are much easier to implement for real-time analysis. However they require a higher computational cost [38]. The most popular SPM method is the spatial-carrier fringe-pattern analysis method that will be utilized in this master thesis. This technique was first introduced by Takeda et al. [39] using one dimensional Fourier Transform (FT) along one scanning line in 1982 and later extended to two dimensions by Macy [40]. Spatial-carrier technique is still state-of-the-art for real-time phase measurement using interferograms [41].

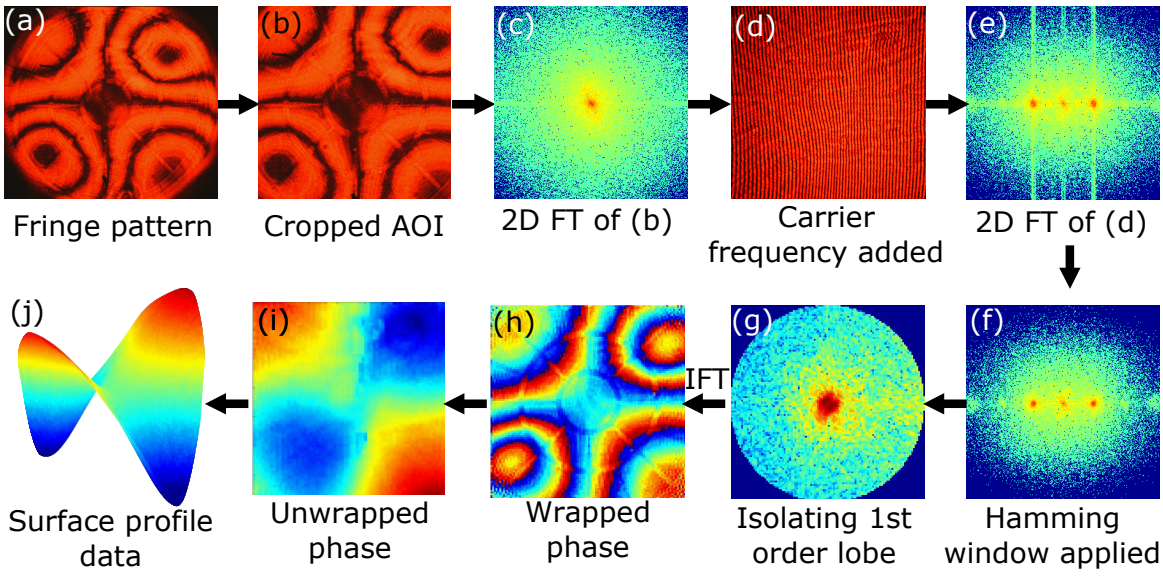

Figure 2.5. Algorithm of the spatial-carrier technique for retrieving surface profile data from an interferogram. All the figures are from actual performed measurements using developed measurement system in this thesis.

Figure 2.5 summarizes the algorithm for performing spatial-carrier technique. If there is no relative angle between the plane mirrors, the interferogram in spatial domain looks like figure 2.5a which shows the distorsions caused by the deformable membrane. The general form of the intensity pattern of an interferogram is given by [38]:

$$I(\mathbf{r}) = D(\mathbf{r})\left[A(\mathbf{r}) + \sum C_n(\mathbf{r})\right] + N(\mathbf{r}), \tag{2.9}$$

where $C_n(\mathbf{r})$ is as follows:

$$C_n(\mathbf{r}) = 0.5 B_n(\mathbf{r}) \exp\left[jn\left(2\pi f_0 \mathbf{r} + \phi(\mathbf{r})\right)\right]. \tag{2.10}$$

$\mathbf{r}$ is the position vector of the point (r, θ) in the interferogram, $n = ..., -2, -1, 1, 2, ...$ is an integer value pertaining the lobe number, f_0 is the spatial-carrier frequency that can be seen in figure 2.5d, $\phi(\mathbf{r})$ is the unknown phase map, $D(\mathbf{r})$ is a mask defining the interferogram area and is 1 inside and 0 outside of the interferogram, $A(\mathbf{r})$ is the background intensity distribution, $B_n(\mathbf{r})$ is the amplitude of the local contrast of the nth lobe pattern and $N(\mathbf{r})$ is the random noise. Taking the FT of the interferogram (equation 2.9) gives:

$$i(\mathbf{f}) = d(\mathbf{f}) * \left[a(\mathbf{f}) + \sum c_n(\mathbf{f})\right] + n(\mathbf{f}), \tag{2.11}$$

where $\mathbf{f}$ is the position vector of spatial frequencies. Figure 2.5c shows the FT of the interferogram shown in figure 2.5b. By adding a large spatial-carrier frequency f_0 by tilting one of the mirrors, the lobes $c_n(\mathbf{f})$ are separated from the background intensity, which stays at the origin. The first order lobe $c_1(\mathbf{f})$, which contains the desired phase data $\phi(\mathbf{r})$, is shifted by f_0 from the origin. This can be seen by comparing figures 2.5c and 2.5e. To compromise for the influence of discontinuity of data at the edges, a 2D analog of Hamming window is applied to the interferogram before taking FT of the data [38]. Improvement can be observed by comparing figure 2.5e and figure 2.5f. The strong vertical lines in the Fourier domain that are caused by edge effects are reduced after applying the Hamming window in figure 2.5f. Next step is to find and filter out the 1st order lobe $c_1(\mathbf{f})$ (see figure 2.5g). To find the appropriate filter position and diameter, the following points are important:

- In the Fourier domain, spectrum of $C_1(r)$ should not overlap with the spectrum of the background intensity $A(r)$ and the higher order lobes.
- The position of the filter has a significant effect on the accuracy of the measurements. Because of the discrete nature of the data, the appropriate position of the filter center might be in between two pixels. Such situations may be alleviated by use of a high resolution sensor or can be compensated by adjusting the carrier frequency or diameter of the filter.

After filtering the 1st order lobe, it is shifted to the origin to remove the carrier frequency. It is worth mentioning that the filtered first lobe is related to the Point Spread Function (PSF) of the system, which is computed by a Fourier transform instead of imaging the wavefront with a lens.

Next an inverse FT is performed to obtain $C_1(\mathbf{r})$. Consequently the wrapped phase, which is the phase fringes constrained in the range $(-\pi, \pi]$, can be calculated as follows:

$$\phi(\mathbf{r}) = \arctan\left(\frac{\mathrm{Im}\left[C_1(\mathbf{r})\right]}{\mathrm{Re}\left[C_1(\mathbf{r})\right]}\right). \tag{2.12}$$

Wrapped phase (figure 2.5h) needs to go through an unwrapping routine to give a continuous phase map. For more details regarding the employed unwrapping function refer to [42]. The source code of this function can be found in [43]. With the derived

phase map $\phi(\mathbf{r})$ (figure 2.5i), it is possible to calculate membrane height h at each point (r, θ) using equation 2.8 (figure 2.5j). The overall obtained accuracy of this method under controlled conditions is proved to be $\lambda/100$ [38]. For a recent reference regarding spatial-carrier technique refer to *Interferogram Analysis for Optical Testing* by Malacara [41, ch. 8].

2.3. Adaptive optics in microscopy

Since invention of telescopes and microscopes there has been a constant quest to improve imaging resolution and contrast and push the limits of image quality to be only limited by wave nature of light [4]. However the resolution of even high-end microscopes is usually affected by the optical properties of the specimen due to inhomogeneity of refractive indices and/or by optical elements. Figure 2.6b demonstrates the aberrations caused by differences in refractive indices. This problem is more pronounced when imaging deep into biological tissues. In order to push forward the depth that can be imaged inside the specimens from only a few cellular layers with acceptable resolution, AO techniques has been employed in microscopy to actively control the wavefronts present in image formation [3]. As it can be seen in figure 2.6c if the aberration is known, it is possible to correct the wavefront before image formation by compensating for the phase distortions. This is achieved by generating the conjugate of the phase of the present aberrations using the wavefront modulator. There are direct and indirect methods of aberration measurement. They are briefly explained in the following subsections.

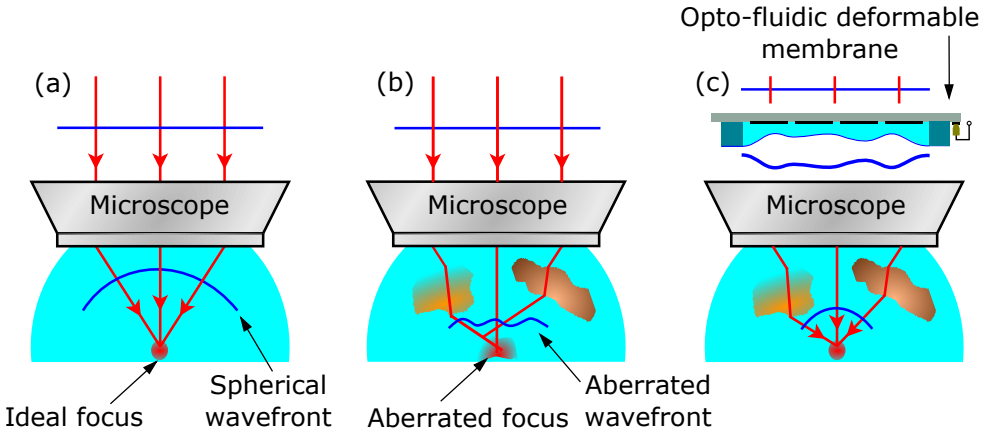

Figure 2.6. Demonstration of the effect of inhomogeneity of refractive indices on the imaging properties of a microscope objective. (a) Formation of an ideal focus in the absence of aberrations. (b) Incoming flat wavefront gets aberrated because of differences in refractive indices. (c) The wavefront is corrected before image formation by applying the conjugate of the phase of the aberrations by help of the wavefront modulator.